Chinese Chemical Letters 35 (2024) 108568

Contents lists available at ScienceDirect

Chinese Chemical Letters

journal homepage: www.elsevier.com/locate/cclet

Cu single atoms embedded on hollow g-C_3N_4 nanospheres with enhanced charge transfer and separation for efficient photocatalysis

Linlin Zhang[a], Jianjun Liao[a,*], Yakun Li[b], Wei Sun[a], Chengjun Ge[a,*]

[a] *Key Laboratory of Agro-Forestry Environmental Processes and Ecological Regulation of Hainan Province, School of Ecology and Environment, Hainan University, Haikou 570228, China*

[b] *Shandong Ocean Chemical Industry Scientific Research Institute, Weifang 262737, China*

ARTICLE INFO

Article history:
Received 10 February 2023
Revised 16 April 2023
Accepted 11 May 2023
Available online 12 May 2023

Keywords:
g-C_3N_4
Cu single atom
Hollow nanospheres
Charge transfer pathways
Photocatalytic hydrogen production

ABSTRACT

Establishing an effective charge transfer mechanism in carbon nitride (g-C_3N_4) to enhance its photocatalytic activity remains a limiting nuisance. Herein, the combination design of a single Cu atom with hollow g-C_3N_4 nanospheres (Cu-N_3 structure) has been proven to offer significant opportunities for this crucial challenge. Moreover, this structure endows two pathways for charge transfer in the reaction, namely, the N atoms in the three-dimensional planar structure are only bonded with a single Cu atom, and charge transfer occurs between the plane and the layered structure due to the bending of the interlayered g-C_3N_4 hollow nanospheres. Notably, Cu-N_3 and hollow nanosphere structures have been certified to greatly enhance the efficiency of photogenerated carrier separation and transfer between the layers and planes by ultrafast spectral analysis. As a result, this catalyst possesses unparalleled photocatalytic efficiency. Specifically, the hydrogen production rate up to 2040 μmol h^{-1} g^{-1}, which is 51 times that of pure C_3N_4 under visible light conditions. The photocatalytic degradation performance of tetracycline and oxidation performance of benzene is also expressed, with a degradation rate of 100%, a conversion of 97.3% and a selectivity of 99.9%. This work focuses on the structure-activity relationship to provide the possibilities for the development of potential photocatalytic materials.

Photocatalysis is a promising new energy conversion technology and pollutant treatment technology [1–4]. Polymeric carbon nitride (g-C_3N_4), as a common organic semiconductor photocatalysts, has been applied in the fields of energy and environmental remediation due to its visible light responsiveness, robust stability, high wear resistance, excellent physicochemical properties and low synthesis cost [5–9]. However, the low charge separation and transfer efficiency of bulk C_3N_4 restrict its further development [10–13]. To overcome the challenge of constraints and enhance unsatisfactory performance, various effective strategies have been probed, such as the establishment of defects, doping of heterogeneous elements, construction of heterojunctions, and nanostructures [14–19]. Nevertheless, it is imperative to develop and use multiple charge transport tunnels.

The ultra-high conductivity metal seems to be the best candidate for modifying g-C_3N_4. In particular, the introduction of atom-sized metals can not only maximize the utilization of metals but also improve the charge separation and transfer efficiency of g-C_3N_4 [20–23]. For example, various noble or non-noble metal single atoms (Au, Pt, Pd, Cu, Co, *etc.*) have been immobilized on g-C_3N_4, because these metal atoms can be anchored at rich N sites [24–26]. The metal atom fixed carbon nitride can effectively improve photocatalytic performance because the atom acts as an effective electron acceptor in the separation and transfer of photogenerated carriers in the plane [27–30]. Thus, the introduction of metal atoms in the g-C_3N_4 plane of the pyrazine (herbicide) conjugate can change the spatial charge transfer pathway [31]. However, in-plane doping alone is insufficient to further promote photocatalytic performance, among which, the most effective challenge is to improve the charge transfer between layers (adjacent layers of g-C_3N_4). This is mainly because the intrinsic planar layered structure of g-C_3N_4 is destroyed along with the weakening of electron transfer in the flat layer [32,33]. The basic understanding is that the electronic structure of g-C_3N_4 consists of sp^2 hybrid π delocalized electrons and lone electrons in N-pz orbit [34,35]. Bending the structure of g-C_3N_4 from the plane structure to the spherical structure will cause the electronic structure to deform and compress in the mixed intermediateness between sp^2 and sp^3, further causing the delocalized π electrons to migrate from the concave to the convex [36,37]. The formation of a hollow spherical struc-

* Corresponding authors.
E-mail addresses: liaojianjun008@163.com (J. Liao), cjge3007@163.com (C. Ge).

https://doi.org/10.1016/j.cclet.2023.108568
1001-8417/

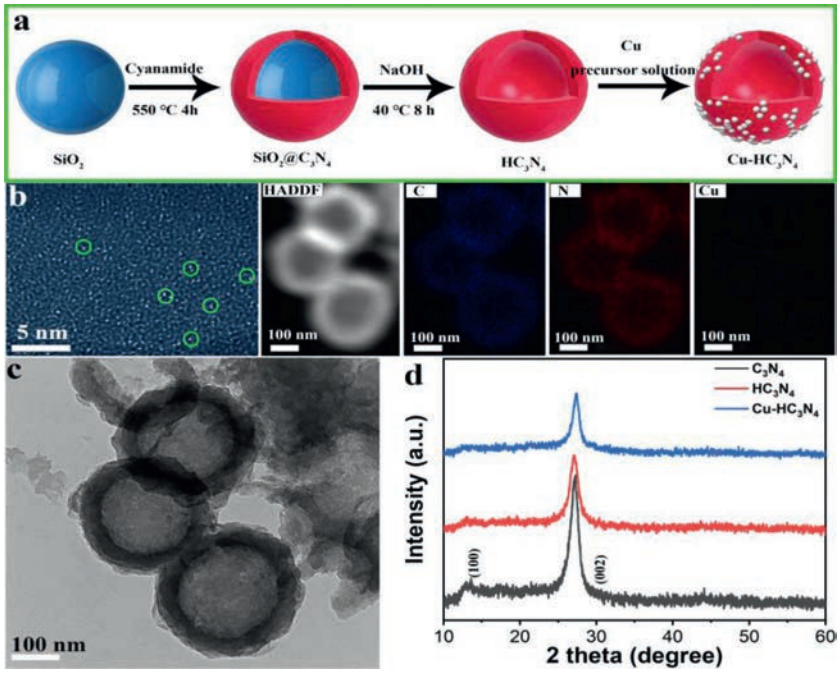

Fig. 1. (a) Scheme of Cu single atom doted HC_3N_4. (b) HAADF-STEM, HADDF, mapping image of Cu single atom HC_3N_4. (c) TEM of Cu-HC_3N_4 composite. (d) XRD patterns for C_3N_4, HC_3N_4 and Cu-HC_3N_4 composite.

ture is an effective method for bending layered g-C_3N_4. This will eventually result in a significant potential difference between the inner and outer surfaces of the g-C_3N_4 hollow nanospheres due to the uneven distribution of electrons. Therefore, the potential difference of g-C_3N_4 hollow nanospheres as the motive power will stimulate the e^- to conquer the electrostatic barrier of the interlayer and shift to the outer layer of g-C_3N_4 hollow nanospheres [38,39]. In addition, the hollow nanosphere structure can enhance the light scattering and photosensitivity of g-C_3N_4 or their composites. In a word, hollow sphere structure is an effective method to improve photocatalytic performance, which has been widely proved.

Therefore, we prepared hollow g-C_3N_4 nanospheres (HC_3N_4) and loaded Cu single atoms as electron acceptors on the surface of Cu-HC_3N_4. Multiple testing methods demonstrated that single Cu atoms were embedded in the C_3N_4 plane, and had an enormous capacity to enhance charge separation and transfer within the plane. The hollow nanosphere structure enhanced charge separation and transfer in the interlayer. Therefore, under visible light irradiation, Cu single atom-modified, hollow g-C_3N_4 nanospheres exhibited excellent performance in the selective oxidation of benzene to phenol and photocatalytic hydrogen evolution. The molecular structure engineering strategy of introducing the bending of the delocalized π electrons of g-C_3N_4 provided a new option for promoting oriented charge transfer between nanolayers and is applicable to other single-atom functional materials.

As shown in Fig. 1a, we used SiO_2 as the hard template to synthesize HC_3N_4 nanospheres by thermal polymerization. Then, monoatomic copper is loaded, and finally hollow carbon nitride loaded with monoatomic copper is formed. Single atoms of copper show bright spots in high resolution high angle ring dark field (HAADF) to determine whether it exists. As shown in Fig. 1b, multiple bright spots with uniform size and uniform distribution are presented, proving that the product contains Cu in the form of a single atom. Furthermore, the synthesized HC_3N_4 is composed of C, N and Cu elements and proved by element mapping. More excitingly, it can be observed that Cu is uniformly distributed on the entire carbon nitride carrier. The loaded copper content was monitored as 0.50 ± 0.02 wt% by inductively coupled plasma atomic emission spectrometry (ICP-AES). As displayed in Fig. S2 (Supporting information), the Cu-HC_3N_4 is the nanospheres structure. Furthermore, it can be seen from the mapping image and Fig. 1c that the prepared sample is a hollow nanosphere structure. And the Cu element is evenly distributed in the hollow spherical shell.

Fig. 1d shows the XRD patterns of HC_3N_4 with Cu single atom loadings, C_3N_4 and HC_3N_4. For C_3N_4, a very distinct XRD diffraction peak situated at 27.7°, which is attributed to the interlayer stacked reflectance of the conjugated aromatic hydrocarbon system [5]. The signature peak at 2θ is the typical (002) peak to indicate the graphite material [40]. Otherwise, for HC_3N_4, the peak with intensity slightly higher than the noise appears at 2θ of 13.3°, showing an in-plane repeated structural unit of tri-*s*-triazine. It can be seen that compared with C_3N_4, hollow g-C_3N_4 nanospheres have a less porous and layered structure. Compared with the former two, there is almost no (100) peak in Cu-HC_3N_4, which proves that the aromatic structure is destroyed [9]. Fig. S3 (Supporting information) gives the FTIR spectroscopy to clarify the structural composition of the synthesized photocatalyst. It is obvious that all the synthesized photocatalysts display the analogous FT-IR signals. Specifically, the characteristic peak loaded at 813 cm^{-1} represents the condensed heptazine heterocyclic ring (C_6N_7). The peaks at 1545 cm^{-1}, 1328 cm^{-1}, and 1232 cm^{-1} correspond to C=N(sp^2), C–N(sp^2) in the heptazine unit and the C–NH–C bond in melamine, respectively, which prove the composition of the basic heptazine unit of g-C_3N_4 [41–45]. The pronounced broad spectral band is in the range of 3000–3800 cm^{-1}, which is mainly due to the N–H band formed by the uncondensed amine group and the ·OH formed by the adsorption of H_2O on the surface [5].

X-ray absorption spectroscopy (XAS) was used to determine the valence structure and coordination environment of Cu in the synthesized Cu-HC_3N_4 sample. As displayed in Fig. 2a, the absorption edge of the Cu-HC_3N_4 sample is located between the absorption edges of CuO and Cu_2O (Cu K-edge X-ray absorption near edge structure spectrum, XANES), demonstrating the presence of Cu^+ (the predominant oxidation state) and Cu^{2+} in Cu-HC_3N_4 [20,31]. The absorption edge of the Cu-HC_3N_4 migrated to a higher energy than that of Cu foil, indicating that Cu is oxidized in Cu-HC_3N_4

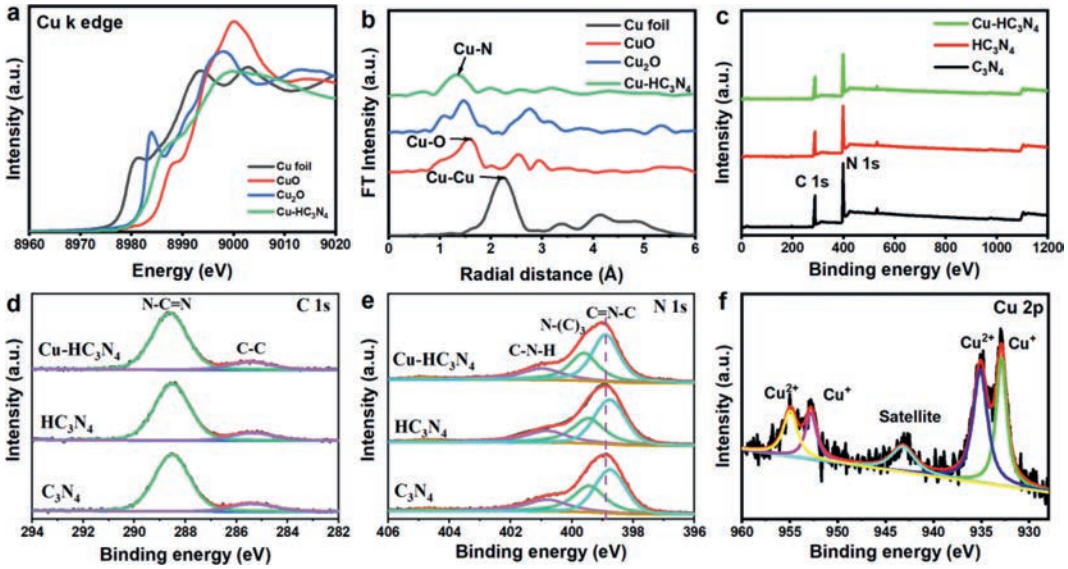

Fig. 2. (a) Cu K-edge XANES spectra. (b) FT-EXAFS spectra. (c) XPS survey spectra and corresponding high-resolution XPS spectra of (d) C 1s, (e) N 1s and (f) Cu 2p.

[26]. The FT value of the EXAFS results at the Cu K edge shows that a distinct symmetrical peak of the Cu foil at ≈2.2 Å is attributed to the Cu-Cu bond (Fig. 2b), which is not found in Cu-HC_3N_4. On the contrary, a very obvious peak appears at ≈1.4 Å, which is attributed to the Cu-N bond. The chemical structure of the Cu-HC_3N_4 sample was further determined by X-ray photoelectron spectroscopy (XPS). Fig. 2c presents the survey XPS spectra of all synthesized material, and it is detected that the material has two characteristic peaks of C and N elements. It is worth noting that a slight or negligible Cu signal is present in Cu-HC_3N_4 material, proving that the Cu element content in the sample is low. Two significant characteristic peaks of 284.8 and 288.3 eV appeared in the C 1s high-resolution XPS spectrum (Fig. 2d), indicating the presence of C–C and sp^2 bond carbon (N–C=N) in the g-C_3N_4 skeleton, respectively [9]. The high-resolution spectrum of N 1s shows characteristic peaks at 401.3, 400.2, and 398.6 eV in the g-C_3N_4 sample (Fig. 2e), corresponding to graphical nitrogen, pyrrole nitrogen, and pyridine nitrogen, respectively [9]. Not surprisingly, the N 1s binding energy of Cu-HC_3N_4 is slightly higher than that of C_3N_4, indicating the slight decrease in the electron density of the pyridine N atom, which is attributed to its interaction with the Cu atom. Hence, the Cu atom is immobilized on the pyridine N atom in g-C_3N_4 to form a stable structure. For Cu-HC_3N_4, in the Cu 2p high-resolution spectrum, in addition to containing Cu^+, it also shows two characteristic peaks of Cu^{2+} corresponding to 935.0 and 955.0 eV, and the ratio of Cu^{2+} to Cu^+ is ∼2 (Fig. 2f) [28]. The above results indicate the existence of single-atom copper.

The optical properties and light harvesting ability of C_3N_4, HC_3N_4 and Cu-HC_3N_4 were studied by UV–vis diffuse reflectance spectroscopy. As presented in Fig. 3a, the UV–vis absorption edges of all samples are analyzed as follows: The absorption edge of C_3N_4 is located at 458 nm, while the HC_3N_4 and Cu-HC_3N_4 are red-shifted to 465 and 468 nm, respectively. In addition, all materials show tailing absorption in the visible region, which is attributed to the Cu single atom and hollow structure. The reaction of Cu atoms on the surface properties of hollow g-C_3N_4 nanospheres was investigated by N_2 adsorption tests. As shown in Fig. 3b, HC_3N_4 and Cu-HC_3N_4 samples express the traditional type IV isotherms and have high adsorption capacity, especially at high ($P/P_0 > 0.8$) relative pressure. The BET specific surface areas of HC_3N_4 and Cu-HC_3N_4 samples are 45.2 and 100.4 m^2/g, which are 4.8 and 10.6 times that of g-C_3N_4 (9.4 m^2/g), respectively. The Cu-HC_3N_4 sample with such a high specific surface area is derived from its unique hollow nanospheres morphology, which provides more active sites for utilization.

As shown in Fig. 3c, a significant photoluminescence (PL) quenching occurs in the steady-state PL emission spectra of the Cu-HC_3N_4 heterostructure relative to Cu-C_3N_4, HC_3N_4, and C_3N_4, indicating the intrinsic radiative recombination of the photogenerated electron-hole pairs in C_3N_4, HC_3N_4, and Cu-C_3N_4. It follows that the PL quenching on C_3N_4 and HC_3N_4 may be caused by the introduction of Cu atoms. In addition, compared with C_3N_4, the PL intensity of HC_3N_4 also decreases, which indicates that C_3N_4 can effectively improve the charge transport between the interface layers after surface bending *via* hollow structure, and effectively inhibit the carrier recombination. Furthermore, as seen in Fig. 3d and Table S4 (Supporting information), the time-resolved transient PL decay spectra by the position of the corresponding steady-state emission peaks show that the Cu-HC_3N_4 heterostructure has a longer charge carrier average lifetime (τ_{avg}) relative to Cu-C_3N_4, HC_3N_4, and C_3N_4, which indicates the presence of more efficient charge transfer in Cu-HC_3N_4. By using a pump pulse at 400 nm wavelength, electrons are effectively promoted from the valence band to the conduction band of g-C_3N_4. As shown by the results, a very similar TA spectrum characterized by the detection of bleaching signals appears in the detection range of 450–760 nm wavelengths. A global fitting procedure to retrieve the characteristic relaxation time constants was performed to eliminate the avoidable effects of different probe wavelengths on the recovery kinetics. The average time constants for C_3N_4, HC_3N_4, Cu-C_3N_4, and Cu-HC_3N_4 are 112, 93, 86, and 68 ps, respectively, as shown in Fig. S4 (Supporting information). The fit results converge to a long-lived plateau with a certain amplitude, which reflects the longer lifetime of the charge recombination process on the nano-microsecond time scale. And the average recovery lifetime is an obvious indicator to assess the separation/transfer efficiency of photogenerated charge carriers. By comparing the average recovery lifetime cases of HC_3N_4 and Cu-HC_3N_4, a decrease can be observed. This may be due to the fact that Cu-N_3 opens an additional in-plane channel for electron transfer which shortens the average recovery lifetime. There is also a decrease in the average recovery lifetime of Cu-HC_3N_4 compared to Cu-C_3N_4, which may be due to the hollow nanosphere structure opening an additional interlayer channel for electron transfer.

Furthermore, chrono-measured *I-t* curves under chopper illumination conditions were used to characterize the photo-response of C_3N_4, HC_3N_4, Cu-C_3N_4, and Cu-HC_3N_4 catalysts. As shown in

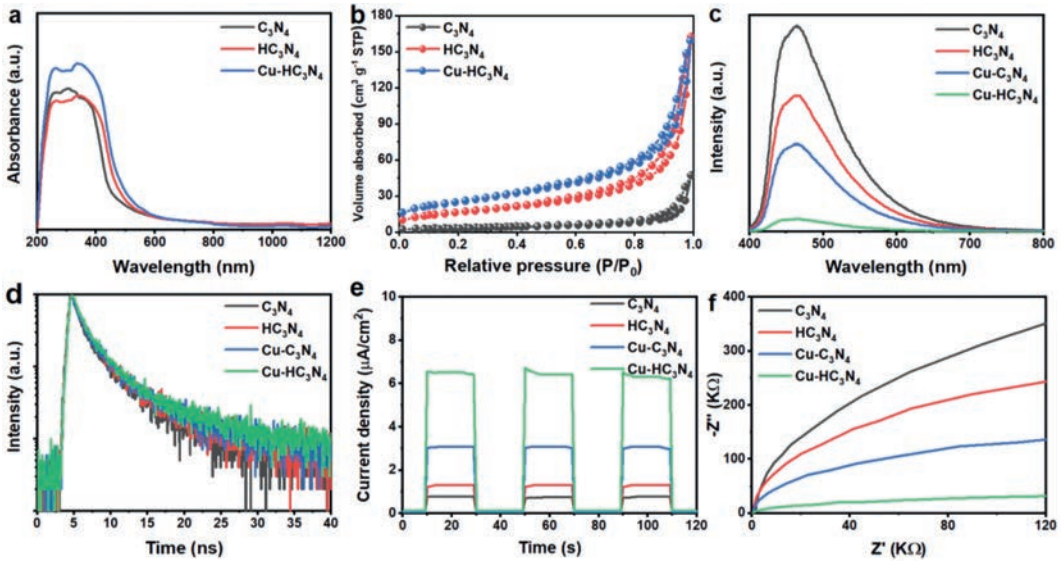

Fig. 3. (a) UV–vis DRS of C_3N_4, HC_3N_4, and Cu-HC_3N_4. (b) Nitrogen adsorption desorption isotherm, (c) steady-state PL spectra, (d) time-resolved PL spectra, (e) transient photocurrent responses and (f) Nyquist plots of C_3N_4, HC_3N_4, Cu-C_3N_4, and Cu-HC_3N_4.

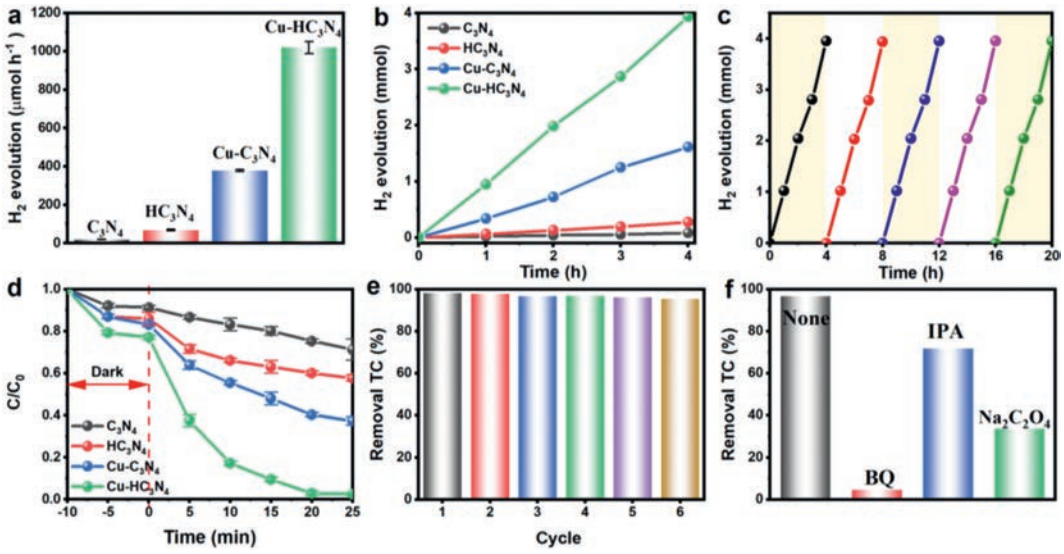

Fig. 4. (a) Average hydrogen production rates and (b) H_2 evolution under visible light irradiation. (c) Cycling tests of photocatalytic hydrogen generation of Cu-HC_3N_4. (d) Photocatalytic TC degradation. (e) Cycling tests of photocatalytic TC degradation of Cu-HC_3N_4. (f) The effects of scavengers on the photocatalytic TC degradation (catalysts = 50 mg, scavenger = 10 mmol/L).

Fig. 3e, the Cu-HC_3N_4 catalyst has a higher photocurrent value relative to the pristine HC_3N_4 and Cu-C_3N_4, indicating that the Cu -HC_3N_4 catalyst has a higher electron-hole separation efficiency. A rapid improvement in charge transfer capability was also confirmed by electrochemical impedance spectroscopy (EIS). The small arc radius of the Nyquist plot of the Cu-HC_3N_4 electrode was used to characterize the rapid interfacial charge transfer between Cu-HC_3N_4 and the dielectric (Fig. 3f). The results shown above further demonstrate that the hollow structure has the positive effect of promoting the separation of photogenerated carriers within the face and between the layers, thereby also improving the performance of single-atom Cu-HC_3N_4 photocatalysts.

The photocatalytic hydrogen evolution experiments were implemented by using methanol as an electron donor and platinum as a co-catalyst under visible light ($\lambda > 420$ nm) irradiation. Hydrogen evolution rates were about 20 μmol/h for C_3N_4, 68 μmol/h for HC_3N_4, 378 μmol/h for Cu-C_3N_4, and 1020 μmol/h for Cu-HC_3N_4 (Figs. 4a and b). Cu-HC_3N_4 has a relatively good activity as a good performing photocatalyst over a longer period of time (Fig. 4c). It is because of the high planar and interlayer conductivity generated by Cu-N_3 and hollow nanostructures, which allow rapid migration of photogenerated electron-hole pairs and inhibit charge recombination, the photocatalytic activity of Cu-HC_3N_4 is higher than that of C_3N_4, HC_3N_4 and Cu-C_3N_4. Besides, the effect of the number of Cu single atoms on the product hydrogen evolution can also be seen by Fig. S5 (Supporting information), where the loading of Cu should not exceed 0.50 wt%, otherwise there is a significant decrease in activity, which is due to the aggregation of copper atoms making the utilization of copper atoms less efficient.

As shown in Fig. 4d, the photocatalytic performance of the Cu-HC_3N_4 sample was verified by tetracycline (TC) photocatalytic degradation in an aqueous solution under visible light irradiation, where the photoelectrons generated by the photocatalyst were transferred to copper ions for efficient copper cycling, enabling the continuation of the reaction. In addition to this, the holes generated by light can also produce certain radicals. Therefore, single-

atom copper and hollow structure modified photocatalytic materials can generate free radicals better due to their higher charge separation properties. Under dark conditions, the adsorption of the model pollutant TC on the surfaces of C_3N_4, HC_3N_4, Cu-C_3N_4 and Cu-HC_3N_4 after 10 min was not different compared to the results of BET. Under visible light irradiation, the absorption intensity of TC decreases with time, indicating the appearance of photo-oxidation of TC, and suggesting that Cu-HC_3N_4 has the best photocatalytic degradation, which is caused by the combined effect of the unitary copper and hollow nanosphere structure. The total organic carbon removal rate is displayed in Fig. S6 (Supporting information), and the results indicate that the removal of organic carbon is similar to the degradation outcomes, with Cu-HC_3N_4 exhibiting the highest removal rate. This suggests that it has superior photocatalytic degradation performance.

The stable photocatalytic performance of Cu-HC_3N_4 was demonstrated by stability testing (Fig. 4e), proving the successful preparation of a single-atom photocatalyst with excellent performance. XRD and FTIR tests were performed for the samples recovered after the test (Fig. S7 in Supporting information). As shown in Fig. S7b, there was no significant change in the spectra before and after the tests, which further verified that the photocatalyst has good stability. Furthermore, as shown in Fig. 4f, it can be seen that BQ has the greatest impact on performance, indicating that $^{\bullet}O_2^-$ is the main reactive oxygen species. As benzene is an important reagent for the synthesis of many chemicals, the photocatalytic oxidation activity of Cu-HC_3N_4 can be tested by whether it can selectively oxidize benzene to phenol, and the conversion of benzene to phenol cannot occur in the absence of the catalyst (Fig. S8 in Supporting information). Compared to C_3N_4, HC_3N_4 and Cu-C_3N_4, the conversion and selectivity of Cu-HC_3N_4 were improved to 97.3% and 99.9%, respectively, under visible light conditions, providing a more excellent performance. The sample recovery was tested after the experiment (Fig. S9 in Supporting information), and Cu-HC_3N_4 also has good stability for phenol production, as evidenced by hydrogen evolution and TC degradation experiments.

In general, the photocatalytic process involves several steps: First, light is absorbed by the prepared Cu-C_3N_4 photocatalyst, generating an excited state called an electron-hole pair. Second, the electron and hole are separated and migrate to a reaction site on the photocatalyst surface, where the hollow sphere structure and Cu single atoms can effectively promote the separation of photogenerated charge carriers (Fig. S10 in Supporting information). Third, the reactant molecules or ions adsorb onto the photocatalyst surface, and the larger specific surface area of the hollow sphere structure can increase the adsorption of reactant molecules. Fourth, the electrons on the photocatalyst surface react with the adsorbed reactant molecules or ions, causing them to undergo redox reactions. Fifth, the products of the redox reactions desorb from the photocatalyst surface, completing the photocatalysis process.

In summary, we propose a simple pre-assembly strategy to prepare porous and hollow nanospheres g-C_3N_4 photocatalysts with unique Cu-N_3 species and high active site accessibility. Interestingly, compared with HC_3N_4 and Cu-C_3N_4, the developed Cu-HC_3N_4 catalyst exhibits excellent photocatalytic performance, especially in the photocatalytic degradation of TC and the selective oxidation of benzene to phenol. The atomically dispersed, anchored peculiar Cu$-N_3$ species is responsible for the prominent catalytic behavior. This study not only affords a neoteric and highly active catalyst for photocatalytic hydrogen production, but also provides a new way to design and fabricate single-atom catalysts in various g-C_3N_4 micro/nanostructures by changing the metal and/or adjusting the structure of pre-organized supramolecular aggregates.

Declaration of competing interest

The authors declare that they have no known competing financial interests or personal relationships that could have appeared to influence the work reported in this paper.

Acknowledgments

This work was supported by the Hainan Province Science and Technology Special Fund (No. ZDYF2022SHFZ094), National Natural Science Foundation of China (No. 22166016), Hainan Provincial Key Research and Development Program (No. ZDYF2020222), and the open-ended fund of Key Laboratory of Agro-Forestry Environmental Processes and Ecological Regulation of Hainan Province (No. AFEPER202205).

Supplementary materials

Supplementary material associated with this article can be found, in the online version, at doi:10.1016/j.cclet.2023.108568.

References

[1] Y. Chen, S. Lan, M. Zhu, Chin. Chem. Lett. 32 (2021) 2052–2056.
[2] S. He, M. Shen, E. Wu, et al., Environ. Sci. Ecotechnol. 9 (2022) 100141.
[3] Y. Long, H. Xu, J. He, C. Li, M. Zhu, Surf. Interfaces 31 (2022) 102056.
[4] X. Wang, H. Jiang, M. Zhu, X. Shi, Chin. Chem. Lett. 34 (2023) 107683.
[5] D. Zhao, Y. Wang, C.L. Dong, et al., Nat. Energy 6 (2021) 388–397.
[6] C. Hu, J. Hu, Z. Zhu, et al., Angew. Chem. Int. Ed. 61 (2022) e202212397.
[7] Y. Li, H. Wang, X. Zhang, et al., Angew. Chem. Int. Ed. 60 (2021) 12891–12896.
[8] Q. Liu, J. Huang, L. Wang, et al., Sol. RRL 5 (2021) 2000504.
[9] T. Zhao, D. Li, Y. Zhang, G. Chen, J. Colloid Interface Sci. 628 (2022) 966–974.
[10] X. Zhao, Y. Fan, W. Zhang, et al., ACS Catal. 10 (2020) 6367–6376.
[11] X. Zhao, Y. You, S. Huang, et al., Appl. Catal. B 278 (2020) 119251.
[12] L. Zhou, Z. Liu, Z. Guan, et al., Appl. Catal. B 263 (2020) 118326.
[13] Y. Geng, D. Chen, N. Li, et al., Appl. Catal. B 280 (2021) 119409.
[14] Q. Zhang, Y. Peng, Y. Lin, et al., Chem. Eng. J. 405 (2021) 126661.
[15] L. Hu, J. Huang, J. Wang, et al., Appl. Catal. B 320 (2023) 121945.
[16] S. Gong, X. Teng, Y. Niu, et al., Appl. Catal. B 298 (2021) 120521.
[17] T. Zhao, Z. Xing, Z. Xiu, et al., ACS Appl. Mater. Interfaces 11 (2019) 7104–7111.
[18] Y. Xu, M. Fan, W. Yang, et al., Adv. Mater. 33 (2021) 2101455.
[19] L. Zhang, Z.Q. Wang, J. Liao, et al., Chem. Eng. J. 431 (2022) 133453.
[20] X. Xiao, Y. Gao, L. Zhang, et al., Adv. Mater. 32 (2020) 2003082.
[21] W. Jiang, Y. Zhao, X. Zong, et al., Angew. Chem. Int. Ed. 60 (2021) 6124–6129.
[22] L. Jiang, Y. Xie, F. He, et al., Chin. Chem. Lett. 32 (2021) 2187–2191.
[23] J. Song, M. Huang, N. Jiang, et al., J. Hazard. Mater. 391 (2020) 122024.
[24] Z. Wang, E. Almatrafi, H. Wang, et al., Angew. Chem. Int. Ed. 61 (2022) e202202338.
[25] F. Chen, L.L. Liu, J.H. Wu, et al., Adv. Mater. 34 (2022) 2202891.
[26] G. Wang, Z. Chen, T. Wang, D. Wang, J. Mao, Angew. Chem. Int. Ed. 61 (2022) e202210789.
[27] E. Zhao, M. Li, B. Xu, et al., Angew. Chem. Int. Ed. 61 (2022) e202207410.
[28] J. Wang, T. Heil, B. Zhu, et al., ACS Nano 14 (2020) 8584–8593.
[29] X. Sun, L. Sun, G. Li, et al., Angew. Chem. Int. Ed. 61 (2022) e202207677.
[30] B. Wu, L. Zhang, B. Jiang, et al., Angew. Chem. Int. Ed. 60 (2021) 4815–4822.
[31] T. Yang, X. Mao, Y. Zhang, et al., Nat. Commun. 12 (2021) 6022.
[32] Z. Lin, Y. Zhao, J. Luo, et al., Adv. Funct. Mater. 30 (2020) 1908797.
[33] H.S. Moon, K.C. Hsiao, M.C. Wu, et al., Adv. Mater. 35 (2022) 2200172.
[34] Y. Li, S. Ouyang, H. Xu, et al., Adv. Funct. Mater. 29 (2019) 1901024.
[35] X. Wu, X. Wang, F. Wang, H. Yu, Appl. Catal. B 247 (2019) 70–77.
[36] Z. Lin, C. Shao, S. Jiang, C. Sun, S. Song, Appl. Catal. B 268 (2020) 118742.
[37] J. Luo, Z. Lin, Y. Zhao, S. Jiang, S. Song, Chin. J. Catal. 41 (2020) 122–130.
[38] L. Zhang, W. Sun, C. Ge, J. Liao, Sol. RRL 5 (2021) 2000639.
[39] Z. Tong, D. Yang, Z. Li, et al., ACS Nano 11 (2017) 1103–1112.
[40] C. Huang, Y. Wen, J. Ma, et al., Nat. Commun. 12 (2021) 320.
[41] Y. Huang, K. Wang, T. Guo, et al., Appl. Catal. B 277 (2020) 119232.
[42] X. Hu, W. Zhang, Y. Yong, et al., Appl. Surf. Sci. 510 (2020) 145413.
[43] Y. Liu, J. Li, B. Zhou, et al., Environ. Chem. Lett. 7 (2009) 363–368.
[44] R. Wang, S. Zhang, H. Chen, et al., Environ. Sci. Technol. 57 (2023) 4050–4059.
[45] M. Du, Y. Zhang, Z. Wang, et al., Sep. Purif. Technol. 298 (2022) 121585.